Journal of Manufacturing Processes 146 (2025) 30–43

Contents lists available at ScienceDirect

Journal of Manufacturing Processes

journal homepage: www.elsevier.com/locate/manpro

Impact of interpass temperature on the microstructure and mechanical properties of super duplex stainless steel in CW-GMA additive manufacturing

P. Poulain [a,*], J. Wang [a,*], S. Bouvier [b], S. Williams [a], S. Budnyk [c], A. Gavrilovic-Wohlmuther [c]

[a] Welding and Additive Manufacturing Centre, Cranfield University, Cranfield MK43 0AL, UK
[b] Université de technologie de Compiègne, Roberval (Mechanics, energy and electricity), Centre de recherche Royallieu, CS 60 319, 60 203 Compiègne Cedex, France
[c] Christof Group SBN, Schoeller-Bleckmann Nitec GmbH, 2630 Ternitz, Austria

ARTICLE INFO

Keywords:
CW-GMA additive manufacturing
Super duplex stainless steel
Interpass temperature
Microstructure
Mechanical properties

ABSTRACT

This study investigates the influence of interpass temperature (IPT) on microstructure evolution and mechanical properties of super duplex stainless steel (SDSS) manufactured by cold wire gas metal arc (CW-GMA) additive manufacturing. Thermal cycle analysis showed that cooling rates were not significantly affected by IPT under constant process parameters. However, higher IPTs resulted in higher thermal accumulation and extended exposure to elevated temperatures. Microstructural characterisation revealed the transformation of δ-ferrite grains into various austenitic phases and secondary chromium nitrides during cooling. Fine, needle-like secondary austenite formation was more pronounced at higher IPTs, driven by chromium nitride precipitation near layer transitions. Mechanical testing demonstrated consistent ultimate tensile strength around 810 MPa across IPTs, with ductility variations attributed to porosity. Hardness profiles were uniform, averaging approximately 300 Hv. These findings suggest that while IPT influences thermal accumulation and microstructural details, its effect on ferrite-to-austenite ratio and mechanical properties is minimal. Optimising IPT remains essential for increasing the productivity of SDSS in CW-GMA additive manufacturing.

1. Introduction

Additive manufacturing (AM) has emerged as a promising alternative to traditional manufacturing technologies such as casting, forging, and machining. It enables the production of complex geometries with high precision and minimal material waste, making the process both cost-effective and sustainable [1–3]. Among AM technologies, directed energy deposition (DED) stands out for its ability to build large and complex metal components using a layer-by-layer approach, where material feedstock (e.g. wire or powder) is fed and melted by an energy source (e.g. laser, electron beam, or electric arc) [4]. Wire direct energy deposition (WDED) has shown considerable promise due to its high deposition rates and low material loss, which are especially advantageous when manufacturing medium to large-scale components [5]. Cold wire gas metal arc (CW-GMA) is a new electric arc-based process based on the extensively used GMA technique, with the difference that an additional wire, called the cold wire, is added to the arc. Feeding a cold wire into the melt pool allows better control over the deposition process, thereby reducing heat input and improving energy efficiency [6]. This approach makes CW-GMA an ideal candidate for applications requiring precise control over the thermal input and material properties, mainly when working with advanced alloys such as stainless steels [7].

Super duplex stainless steel (SDSS) is a highly attractive alloy due to its remarkable mechanical strength, toughness, and excellent corrosion resistance. Its microstructure consists of an approximately equal ratio of ferrite and austenite phases, providing superior properties to standard austenitic or ferritic stainless steels [8,9]. These characteristics make SDSS ideal for use in highly corrosive environments, such as in the oil and gas, chemical, and marine industries, where the material is subjected to both mechanical stress and aggressive corrosive agents [10]. Traditionally, SDSS components are produced through casting, forging, and machining. These processes involve complex deformation and shaping techniques, which require precise control of parameters to ensure the desired mechanical properties and microstructural balance. In the case of forging, poor mould design can lead to significant deformation with the risk of cracking or failure during forming due to

* Corresponding authors.
E-mail addresses: paul.poulain@cranfield.ac.uk (P. Poulain), jun.wang.123@cranfield.ac.uk (J. Wang).

https://doi.org/10.1016/j.jmapro.2025.04.091
Received 11 February 2025; Received in revised form 22 April 2025; Accepted 30 April 2025
Available online 1 May 2025
1526-6125/© 2025 The Authors. Published by Elsevier Ltd on behalf of The Society of Manufacturing Engineers. This is an open access article under the CC BY license (http://creativecommons.org/licenses/by/4.0/).

pressure or flow not being matched to the metal [11]. Additionally, these conventional techniques often lead to high material wastage and are less efficient when producing complex geometries, making them less favourable for large-scale SDSS structures. Studies have demonstrated that components produced through AM processes exhibit superior corrosion resistance compared to their wrought counterparts. This improvement is partly due to the redistribution and refinement of alloying elements during the AM process, which enhances the material's protective properties [12].

Despite the advantages of AM in producing DSS components, several challenges remain. While the overall corrosion resistance of AM-processed DSS is good, studies have shown either anisotropic or isotropic behaviour in tensile and fatigue tests. This is often attributed to porosity within the material, which weakens its resistance to cyclic loading and contributes to inconsistent mechanical properties [13,14]. Lack of fusion in AM-processed DSS results from unstable melt pool behaviour or insufficient remelting between. Smaller porosity appeared with low heat input and interlayer temperatures, which can reduce melt pool fluidity and restrict gas escape [15]. Shielding gas composition may result in oxidation or nitrogen loss, contributing to porosity and secondary phase formation [16]. Controlling microstructural parameters remains a key challenge for DSS. The high heat input during the deposition process can disrupt the ratio between ferrite and austenite phases [17,18]. Additional issues include inhomogeneous grain distribution and the formation of undesirable secondary phases, which can further degrade material performance [19]. The shielding gas used in the CW-GMA process also plays a critical role, as it influences the arc stability, material transfer, and thermal behaviour of the melt pool. Adjusting the gas composition allows further optimisation of the deposition process, enabling better control over the final microstructure and material properties [20]. Various strategies have been proposed to address these challenges, focusing primarily on optimising process parameters and implementing post-heat treatments. Lervåg et al. [21] investigated the impact of heat input ranging from 0.40 to 0.87 kJ/mm and found that higher heat input reduced mechanical properties due to an increased austenite volume fraction. Yang et al. [22] investigated the effect of short-duration post-weld heat treatment at temperatures exceeding the secondary phase formation range, demonstrating its effectiveness in regulating ferrite-austenite phase content and improving pitting corrosion resistance. Interpass temperature (IPT) control is a critical aspect of metal AM, mainly due to its direct impact on the thermal history. It affects phase transformations during the cooling cycle, determining the microstructure and, consequently, the final component's mechanical properties and corrosion resistance. In DSS, the cooling rate between 1200 and 800 °C must be carefully regulated to promote the proper formation of austenite from primary ferrite. Additionally, rapid cooling between 800 and 500 °C is essential to prevent the precipitation of detrimental phases, which could negatively affect the material's mechanical properties and corrosion resistance [23]. From an industrial engineering perspective, controlling IPT in AM is directly linked with productivity. Higher IPT reduces the overall cycle time by allowing faster layer deposition. For this reason, some authors have investigated the influence of IPT on phase formation, mechanical properties, and corrosion behaviour in DSS. For example, microstructural evolution under varying IPT conditions has been characterised for the UNS S32750 SDSS alloy [24]. Furthermore, for large structures, the choice of deposition path must be planned with IPT in mind to avoid issues such as excessive heat accumulation or uneven phase distribution. In this study, SDSS single-pass components were deposited using the CW-GMA WDED process. The influence of IPT (75 °C, 200 °C and 350 °C) on microstructure, phase ratio and mechanical properties were systematically investigated. The results from this work will provide new insights into achieving high productivity and high performance in AM of SDSS.

2. Experimental

2.1. Raw materials and CW-GMA setup

The feedstock material is commercially available UNS S32906 (SAF 2906, EN 1.4477) SDSS wire spools with a wire diameter of 1.2 mm. The substrate used in the deposition process is the same as the wire in rolled condition with dimensions of 300 mm × 50 mm × 8 mm. The chemical composition of the filler wires and base material is presented in Table 1.

The CW-GMA setup is shown in Fig. 1(a). A Fronius Advance 4000R power supply was used to generate the electric arc, with an integrated VR 7000 CMT wire feeder supplying the hot wire. The GMA torch was mounted on a 6-axis Kuka robot. Fig. 1(b) illustrates the configuration of the cold wire and GMA torch. In the CW-GMA process the electric arc is triggered and sustained by the hot wire, which is fed and energised through the power supply. The cold wire is added in the arc from an external TEC FEED 40 wire feeder without being energised. A fume extractor ESTA SRF K-15 FM was used during the deposition. The deposition process was instrumented to record variations in current and voltage throughout the buildup with an AMV4000. The thermal cycles during the entire deposition process were recorded using R-type thermocouples placed in holes drilled beneath the substrate, which are 4 mm away from the deposition path. Temperature-time data were recorded and analysed using LabVIEW software. All walls were deposited without substrate preheating. To evaluate the influence of IPT, three single-pass walls were deposited at IPTs of 75 °C, 200 °C, and 350 °C. The walls are designed to be 200 mm in length and consist of 12 layers. Deposition parameters included an energy input of 0.720 kJ/mm, a torch travel speed of 0.6 m/min and a contact-to-work distance (CTWD) of 16 mm, the distance between the contact tip and the material under the torch. The deposition rate for this work is around 7 kg/h. A shielding gas mixture of argon with 2.5 % CO_2 was employed throughout all experiments, with a torch gas flow rate of 20 L/min and a local shielding gas flow rate of 80 L/min. These parameters were carefully selected to ensure consistent deposition quality and process stability.

2.2. Characterisation

Cross-sectional samples, each 5 mm thick, were extracted from the middle of each wall for macrostructural and microstructural analysis. Optical microscopy (OM, Zeiss Stemi 508 for macrostructure and Zeiss Axiolab 5 for microstructure) and electron backscatter diffraction (EBSD, Tescan S8000G SEM) were utilised for characterisation. The samples were hot-mounted and ground using SiC papers starting from 80 grit to 4000 grit, followed by mirror polishing with 3 μm and 1 μm diamond suspensions. For EBSD, an additional fine polishing step using colloidal silica was employed to ensure high surface quality. The polished surfaces were electro-etched using a 40 wt% NaOH solution at 3 V DC to reveal the ferritic and austenitic microstructures.

Microhardness measurements were taken along the building direction of the sample using an Innovatest Falcon 503 micro-Vickers hardness testing machine, applying a 0.5 kg load for 10 s. Indentations started from 0.5 mm from the top and were spaced 0.5 mm apart. Three tensile test coupons were extracted from each wall along the travel direction (TD), with dimensions (refer to ASTM E8) [25] and positions shown in Fig. 2. Tensile tests were conducted using an Instron 4467 30kN electromechanical frame at a 1 mm/min loading rate and room temperature. Fracture morphology was examined using a scanning electron microscope (SEM, Vega Large 3) to understand the fracture mechanism.

3. Results and discussions

3.1. Thermal history

In AM processes, the thermal cycle significantly affects the

Table 1
Chemical composition (wt%) of the filler wires and substrate.

Elements	C	Cr	Ni	Mo	Mn	N	Si	Cu	P	Fe
UNS S32906	0.017	29.9	6.57	2.18	0.95	0.38	0.36	0.14	0.018	Bal.

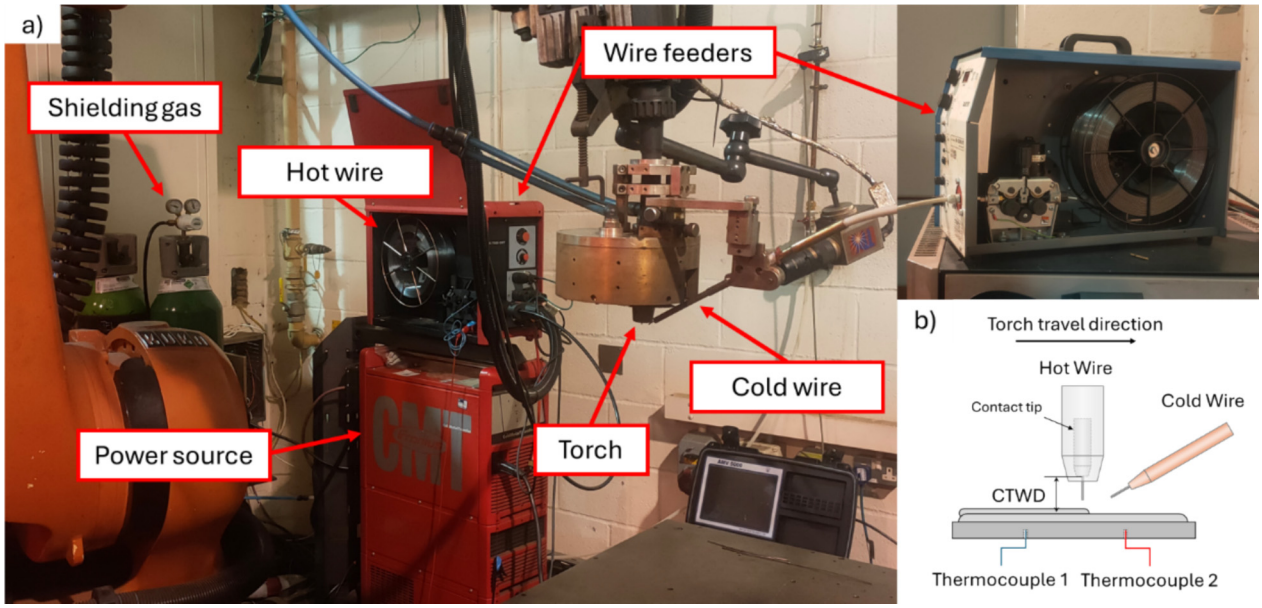


Fig. 1. a) CW-GMA Experimental setup.
b) Illustration of CW-GMA wires and thermocouple position.

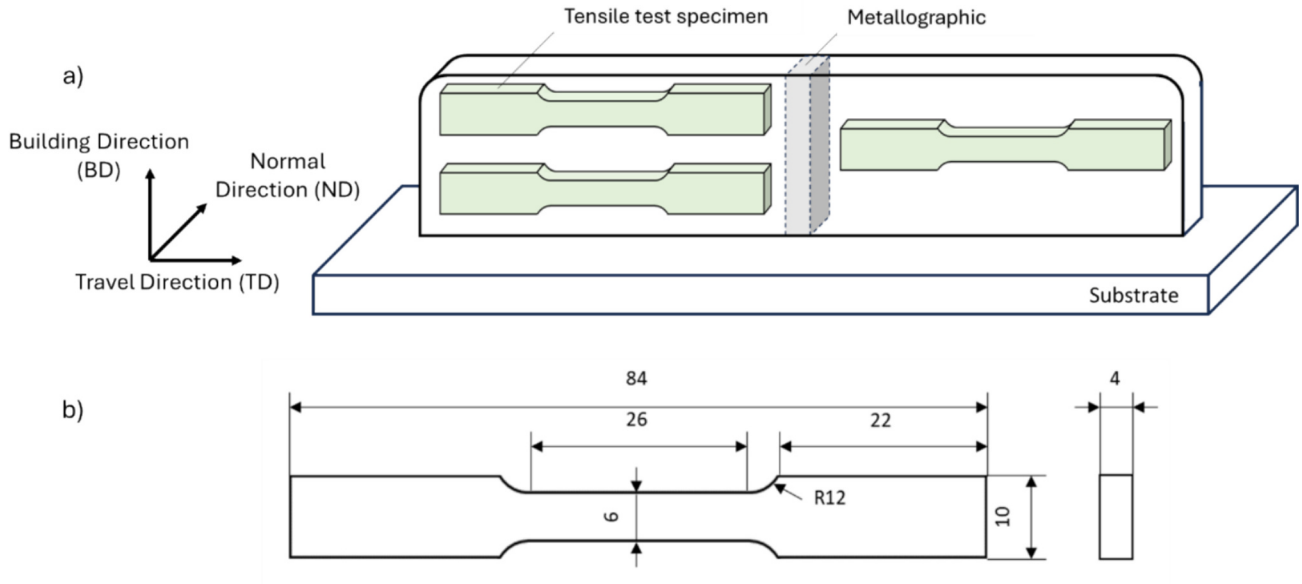


Fig. 2. a) Illustration of the CW-GMA walls with the location of specimens used for uniaxial tensile.
b) Tensile specimen dimensions.

microstructure by influencing solid-state transformations and grain size during cooling [26,27]. The thermal history of the SDSS process using the CW-GMA technique is illustrated in Fig. 3(a), which shows the heating and cooling temperature profiles for each pass. Each temperature peak corresponds to the arc passing over the thermocouple. As additional layers are deposited, the increasing distance between the arc and the thermocouple results in progressively lower peak intensities. In addition, mechanically, the increase in IPT significantly reduces the interpass' dwell time from over 20 min at 75 °C to just 3 min at 350 °C. Reduced dwell time improves manufacturing efficiency, making higher IPTs attractive for industrial applications. Fig. 3(b) presents the average cooling rates between 800 °C and 500 °C ($\Delta T_{8/5}$) for each pass under different IPT conditions, as this temperature range is known to influence microstructural evolution. A consistent $\Delta T_{8/5}$ trend is observed across

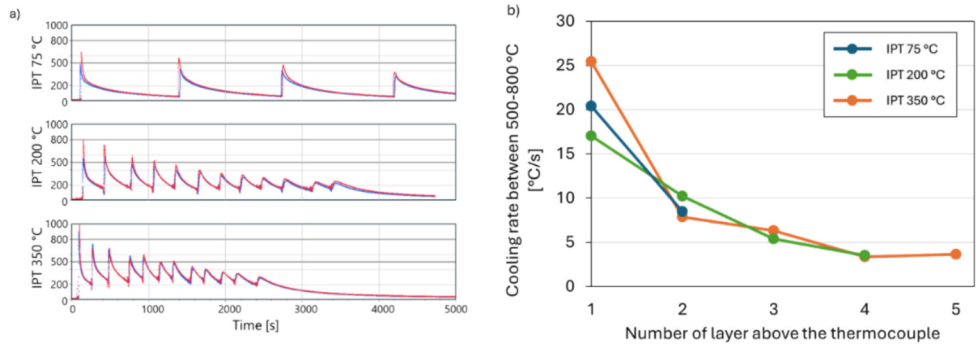


Fig. 3. a) Thermal cycles from the thermocouples; b) Average cooling rates from 800 °C to 500 °C of each pass under different interpass temperature conditions.

IPT conditions when other parameters remain constant, suggesting that the influence of IPT on $\Delta T_{8/5}$ is relatively minor. However, it is important to note that without preheating and with the position of the thermocouples 4 mm below the surface, the thermal profiles obtained may not fully represent the actual temperature conditions closer to the melt pool during steady-state deposition. Given the average layer height of ~2 mm, the first thermocouple reading effectively corresponds to a fictive n + 2 layer. As illustrated in Fig. 3(a), temperatures in the first layer rarely exceed 800 °C and often remain near 500 °C. Higher IPTs progressively raise the minimum temperatures, with peak temperatures recorded above 500 °C for longer durations. This extended exposure to elevated temperatures promotes grain coarsening and phase transformations, impacting the material's mechanical and corrosion resistance properties. However, cooling rates are strongly affected by the deposition process [28] and heat input [29], as these factors modify thermal gradients and solidification behaviour, affecting the microstructure and phase stability. Despite this, higher IPTs lead to temperatures exceeding 500 °C for in-deep layers, up to 5 layers for an IPT of 350 °C.

3.2. *Macro & micro morphology analysis*

Cross-sectional macro morphologies under different IPT conditions are presented in Fig. 4(a–c). Surface waviness is evident in all cases, primarily caused by minor misalignments during the back-and-forth layer deposition process. The wall geometry remains relatively unchanged for IPTs of 75 °C and 200 °C. However, at 350 °C, a noticeable reduction in maximum wall height is observed despite maintaining the

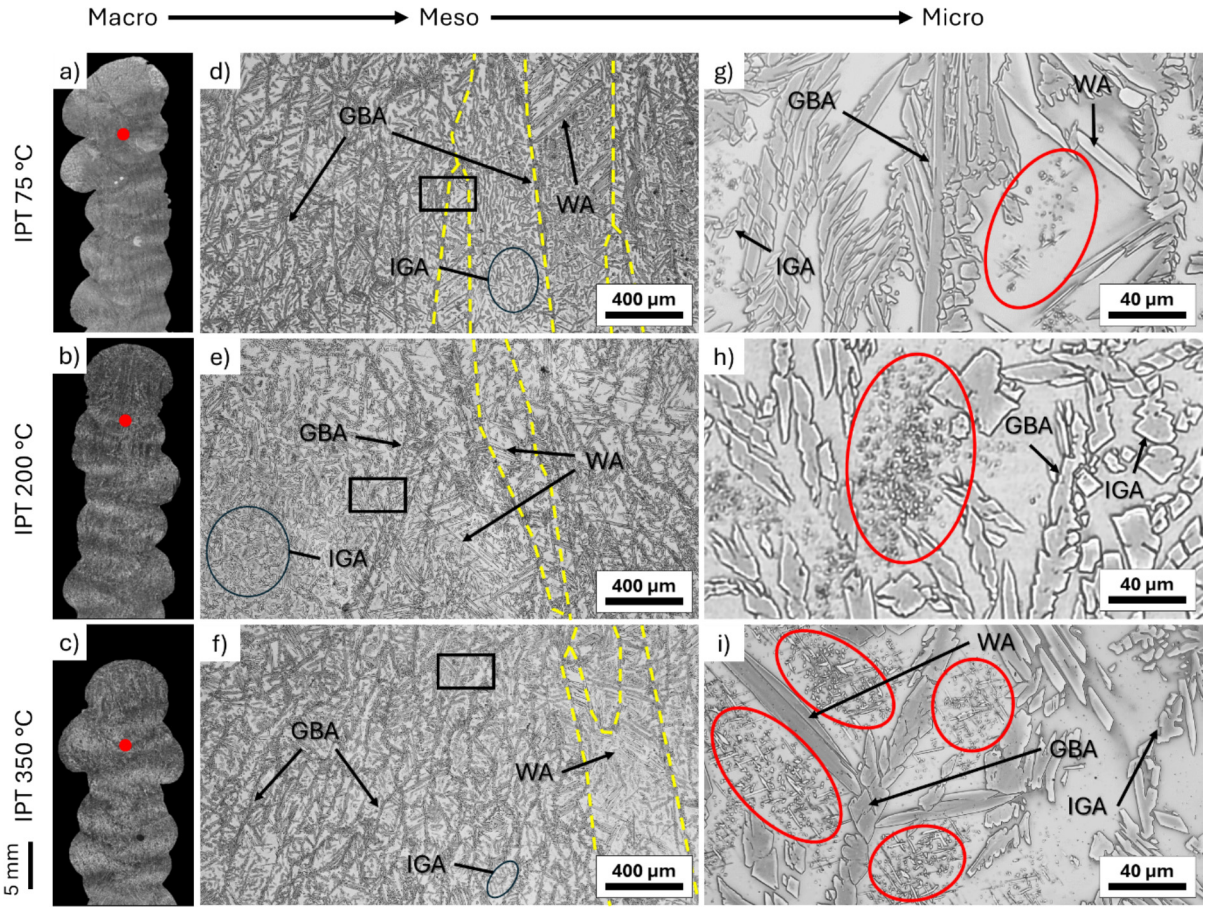


Fig. 4. Cross-section macrographs and microstructure at different magnifications of SDSS CW-GMA walls under different interpass temperatures: (a, d, g) 75 °C; (b, e, h) 200 °C; (c, f, i) 350 °C.

same number of layers and layer thickness. One critical challenge when increasing the deposition rate by reducing interpass dwell time is ensuring the feasibility and formability of the deposited material. Previous studies have shown that significantly higher IPT values can substantially reduce wall height [30]. In addition, with very high IPTs, overflow can easily occur due to a loss of surface tension in the melt pool at the top of the wall. The microstructures in the reheated regions, extending three passes deep, are presented in Fig. 4(d–i). The etching process reveals ferrite as the dark contrast and austenite as the light contrast. At low magnification, Fig. 4(d–f) show that the microstructure across all IPTs exhibits a balanced distribution of δ-ferrite and γ-austenite, forming a ferritic matrix interspersed with various austenitic phases. These phases include grain boundary austenite (GBA), Widmanstätten austenite (WA), and intragranular austenite (IGA), predominantly located within the large columnar ferrite grains aligned along the building direction (BD) highlighted with dashed yellow lines. This alignment is driven by the steep temperature gradient during deposition, which promotes the growth of long columnar ferrite grains as also noted in [31]. These columnar grains are interspersed with zones where the grain size decreases, forming an equiaxed ferritic structure with a grain size of approximately 200 μm. These zones correspond to the fusion lines (FLs) between layers, as shown in the close-up view in Fig. 4(g–i). In these regions, the formation of secondary austenite is observed, and its nucleation and growth increase with higher IPT. At 75 °C, secondary austenite appears as isolated fine grains within the ferritic regions, as indicated by the red circle. With increasing to 200 °C, these precipitates increase in both size and quantity. By 350 °C, secondary austenite evolves into larger acicular structures resembling Widmanstätten patterns. Such evolution suggests that higher IPTs accelerate the kinetics of secondary austenite formation by enhancing atomic mobility and diffusion within the ferritic matrix [32,33].

3.3. Grain morphology and orientation analysis

Inverse pole figure (IPF) maps under different IPT conditions are shown in Fig. 5. These maps were acquired in the cross-sectional plane at consistent heights. Fig. 5 (a–c) cover two to three layers, using a 0.5 μm step size over an area of 5 mm × 3 mm. The microstructure in all three maps is characterised by large columnar ferrite grains extending several millimetres along the BD, aligned with the thermal gradient during

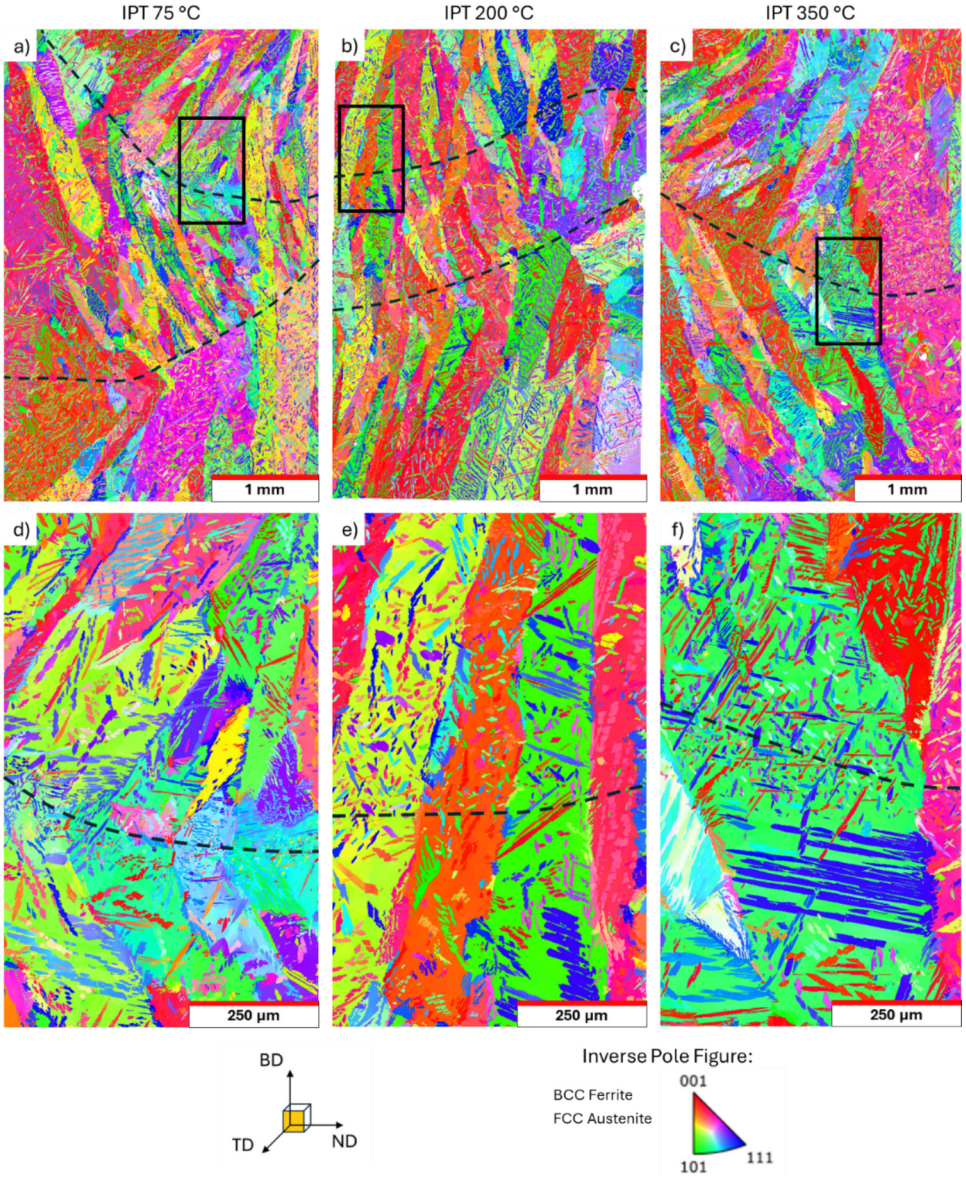


Fig. 5. Inverse pole figures from EBSD analysis of SDSS CW-GMA walls under different interpass temperatures. Low magnification: a) 75 °C, b) 200 °C, c) 350 °C. High magnification: d) 75 °C, e) 200 °C, f) 350 °C.

solidification. Across all IPT conditions, ferrite grains exhibit varying colours, indicating the absence of a dominant crystallographic orientation. This suggests that IPT has minimal influence on the ferrite orientation along BD. The growth of these columnar grains is perpendicular to the FLs, which are highlighted with dotted black lines. Smaller ferritic grains are observed close to the FLs and reveal distinct morphological characteristics depending on IPT. The formation of smaller grains is driven by rapid cooling and localised thermal gradients during layer deposition. At 75 °C, the middle region is dominated by smaller grains between the FLs. At 200 °C and 350 °C, the EBSD maps reveal an increase in the size of ferrite grains near the fusion lines. This coarsening is attributed to prolonged exposure to elevated temperatures, which reduces thermal gradients and enables the grains to grow and develop more stable orientations before depositing additional layers. Fig. 5(d–f) presents high-magnification IPF maps focused on the transition zones between reheated and remelted regions, allowing a more detailed investigation of austenite formation. Complex austenitic morphologies characterise these regions. GBA is observed nucleating along δ/δ grain boundaries, with distinct GBA grains identifiable through changes in crystallographic orientation, even when nucleating along the same pair of ferrite grain boundaries. Lamellar structures of WA extend into the ferrite matrix from the GBA with the same crystallographic orientation as the GBA. This relationship is particularly evident in Fig. 5(f), where a large blue WA colony appears to grow from a GBA region, maintaining a continuous orientation. WA is also observed within large ferrite grains isolated from grain boundaries. However, this may be a result of the 2D cross-section. Despite their apparent isolation, these WA structures exhibit crystallographic orientations closely matching those of nearby GBA and appear constrained by the surrounding ferrite matrix. Pole figure analysis further supports this, revealing a consistent orientation relationship between ferrite and the two austenitic phases. These observations indicate that γ-austenite is influenced by the orientation of the parent δ-ferrite, suggesting an interconnected and orientation-preserving transformation during cooling. Finally, IGA is also observed forming along diffusion fronts, highlighted in the maps with dashed lines.

A detailed examination of EBSD maps, shown in Fig. 6, illustrates the microstructural evolution in the remelted and reheated regions along the height of the sample. The deposition process creates distinct zones: remelted areas, where the material re-solidifies, and reheated regions, which undergo further thermal cycling without complete melting. These regions exhibit notable variations in the size and morphology of austenitic microstructures. Fig. 6(a–c) corresponds to the remelted zone formed by successive layer additions, where the microstructure undergoes a complete reset. A distinct band, marked by yellow lines, becomes visible in the FL region. This band, approximately 100 μm thick, consists of a smaller austenite microstructure with a high concentration of IGA averaging 10 μm in length. In contrast, the reheated regions show significantly larger austenitic microstructures, with some WA reaching up to 400 μm at an IPT of 350 °C. The repeated thermal cycles allow for austenite coarsening. This growth behaviour is similar to that obtained during high-temperature heat treatments [34]. This grain size morphology reflects the complex thermal history experienced by the samples during the additive process along the BD. Variations in cooling rates and thermal accumulation promote differential grain growth. The observed grain size distribution may influence the material properties, as coarser grains in specific regions could impact mechanical strength and corrosion resistance [35]. Based on EBSD phase mapping, the austenite phase content in the 75 °C, 200 °C, and 350 °C sections were measured at 37 %, 34.9 %, and 37.1 %, respectively. The phase ratio analysis indicates no significant variation in the austenite fraction across the different IPTs, suggesting that the IPT has minimal influence on the overall phase distribution under the given process conditions.

3.4. Grain size and distribution analysis

Fig. 7 presents a detailed analysis of the austenitic phase in the remelted and reheated regions through EBSD mapping and grain size characterisation. Fig. 7(a–c) display EBSD maps isolating austenitic structures based on their maximum Feret diameter, with the maps

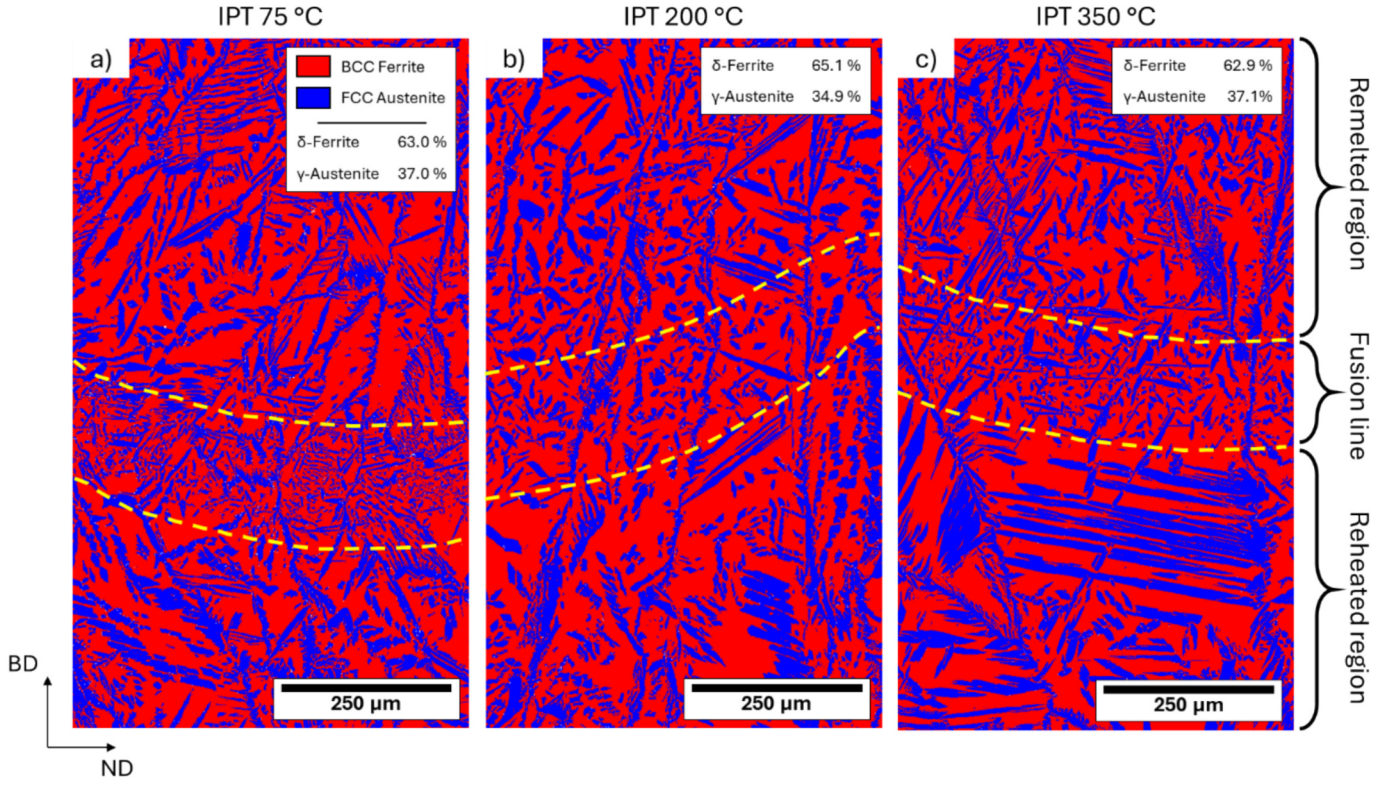


Fig. 6. Phase maps of higher magnification EBSD under different interpass temperatures: a) 75 °C; b) 200 °C; c) 350 °C.

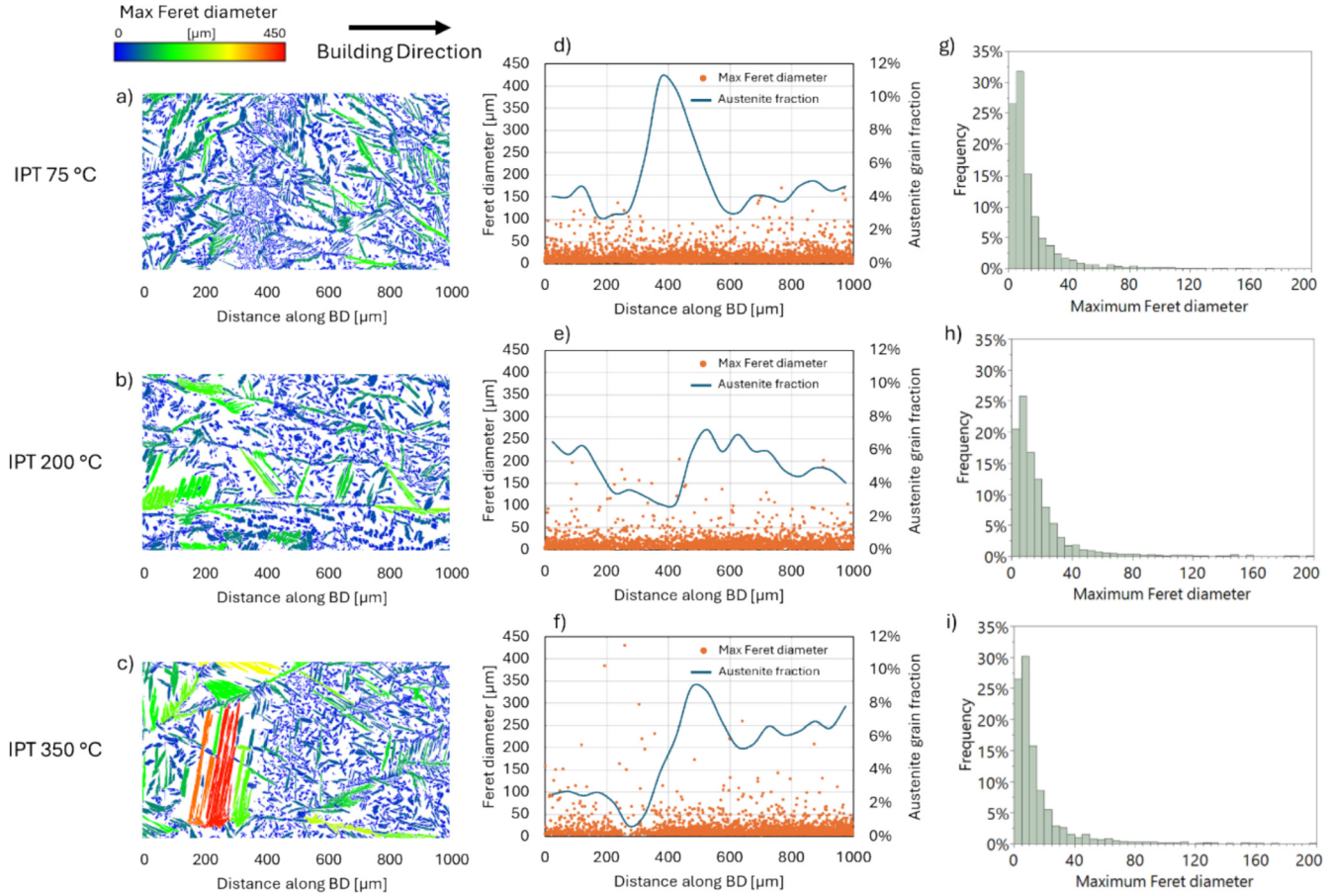


Fig. 7. Austenite phase size analysis at layer transition. a–c) EBSD Maximum Feret diameter d–f) Austenite phase size across the fusion line g–i) Maximum Feret distribution.

oriented such that the BD is aligned to the right. GBA appears fragmented and remains below 200 μm in length despite being concentrated around the periphery of ferritic grains. In contrast, WA exhibits extensive growth as IPT increases, particularly in the reheated region, where extended thermal exposure facilitates its development. GBA typically nucleates along δ/δ boundaries and adopts a crystallographic orientation aligned with one of the two adjacent ferritic grains, often following Kurdjumov–Sachs or Nishiyama–Wassermann relationships [36]. This fixed orientation, established at high temperatures, serves as a foundation for the subsequent growth of WA at lower temperatures. Fig. 7(d–f) illustrate the correlation between grain size, expressed as maximum Feret diameter (orange points), and the spatial position of grains along the BD axis. The data clearly show an increase in the maximum size of austenitic microstructures with IPT, ranging from 180 μm at 75 °C to 450 μm at 350 °C. This growth trend is particularly pronounced near the reheated regions, where the extended thermal exposure associated with higher IPTs promotes grain coarsening. The overlapping phase fraction curves further indicate a local increase in the austenite phase fraction at the FL, suggesting the concentration of austenitic structures in these regions due to localised thermal effects and reheating cycles. Fig. 7(g–i) demonstrate that the majority of austenitic microstructures remain below 40 μm in size, with 93 % of grains falling within this range at IPTs of 75 °C and 200 °C, and 92 % at 350 °C. This indicates that the increase in austenite size is not uniform across the sample, which can be attributed to the large number of smaller austenitic structures in the remelted region. The most pronounced effects of IPT are observed in the reheated region, where extended thermal exposure promotes localised grain growth.

3.5. Crystallographic texture analysis

Ferrite and austenite pole figures (PFs) were constructed for each IPT condition, as shown in Fig. 8. Fig. 8(a, c, e) present the {100} PFs orientation distribution of the BCC δ-ferrite phase. The major axis orientation differs between the samples, with a tilt of 30° for 75 °C and 10° for 350 °C from the BD. This variation is likely due to deposition misalignment and aligns with the δ-ferrite columnar grain direction observed in the EBSD maps. Based on this, the maximum pole intensity can be identified as the tilted {100} ⟨001⟩, as illustrated in Fig. 8(c). The maximum pole intensities for the three IPT conditions were 10.96, 11.40, and 13.81, respectively, indicating that the IPT had minimal influence on the overall texture intensity. The higher texture intensity observed at 350 °C IPT may be attributed to the larger grain size in this condition. Larger grains reduce the number of grains counted within the same analysed area, which can concentrate the pole figure intensity, leading to an apparent increase in texture strength. The {100} and {110} pole figures for the FCC γ-austenitic phase can also be analysed, as shown in Fig. 8(b, d, f). The Kurdjumov–Sachs orientation relationship is visible in the {100} pole figures Fig. 8(b1, d1) as intensity clusters spaced 45° apart. This suggests that austenite nucleates and grows epitaxially on ferrite, inheriting its crystallographic orientation during solidification or phase transformation [37]. The consistent observation of this relationship across IPTs highlights the stability of the epitaxial growth process under varying thermal conditions. Austenite exhibited significantly lower intensity, reflecting more distribution of orientations. The slight decrease in texture intensity at higher IPTs (from 4.14 to 2.64) may reflect minor changes in nucleation dynamics or thermal gradients [38].

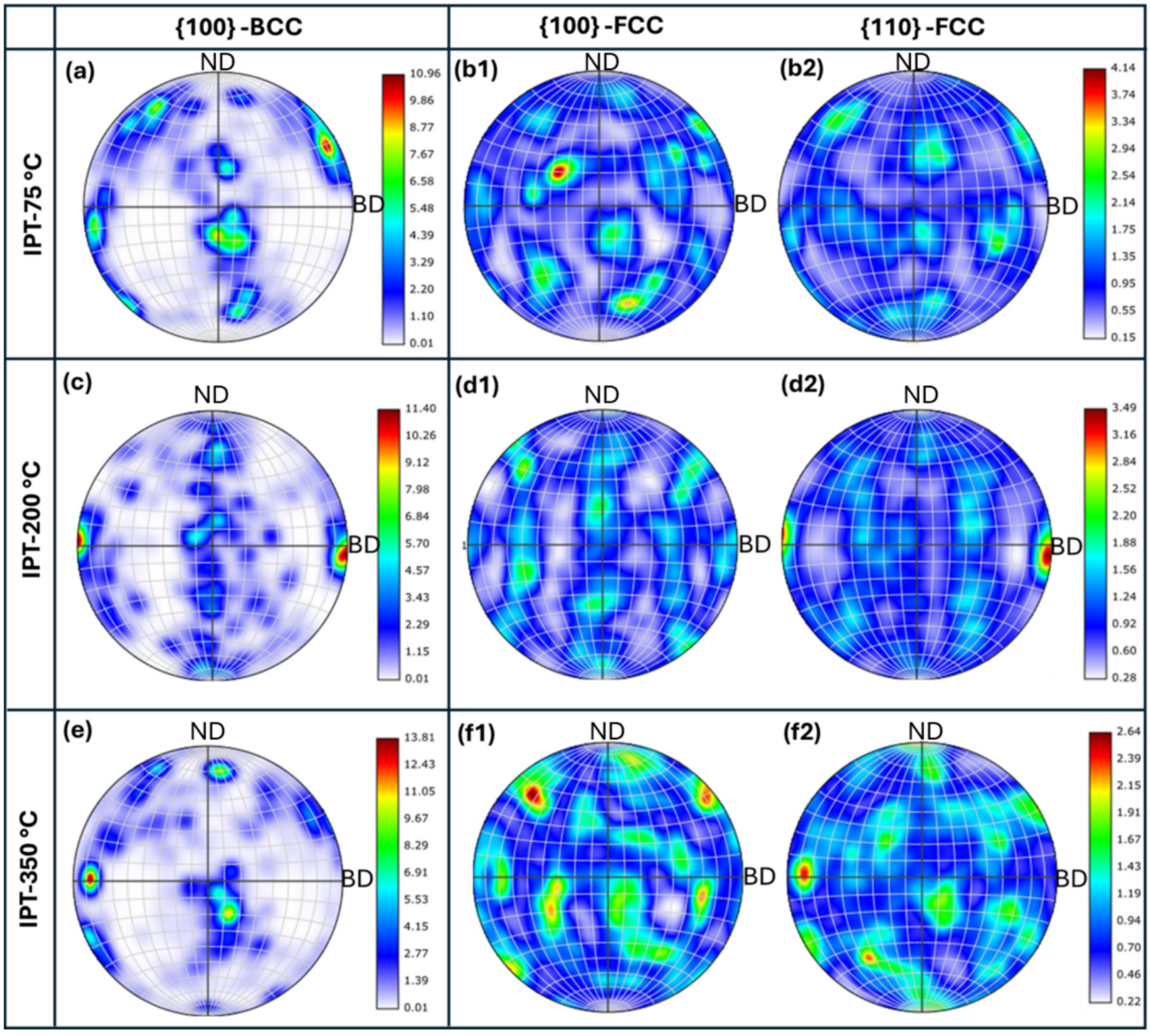


Fig. 8. Phase pole figures for {100} BCC ferrite (a, c, e), {100} FCC austenite (b1, d1, f1), and {110} FCC austenite (b2, d2, f2), oriented along the normal direction (ND) and building direction (BD) for SDSS processed via CW-GMA under interpass temperatures.

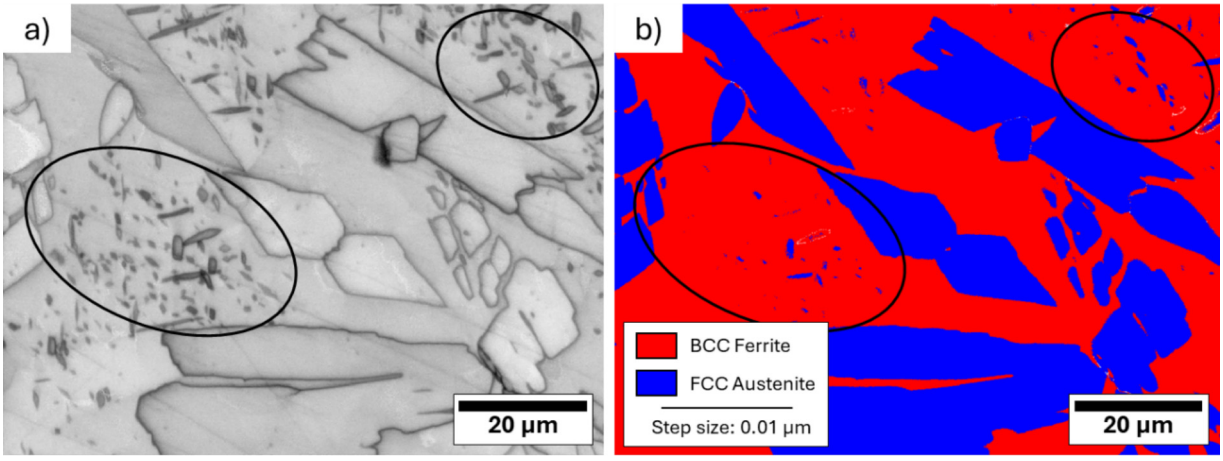


Fig. 9. Secondary austenite identification by EBSD a) Band contrast b) IPF map.

3.6. Secondary austenite and chromium nitrides analysis

Contrary to expectations, variations in IPT did not significantly increase the volumetric fraction of austenite detected by EBSD phase mapping [39]. However, as discussed in 3.2, secondary austenite was found to increase in size with higher IPT, particularly in reheated regions. To further investigate the stability of the phase ratio over different IPTs, a closer examination of secondary austenite formation was conducted at a finer step size of 0.01 μm, as shown in Fig. 9. Fig. 9(a) presents band contrast imaging, highlighting differences in electron backscatter intensity across the sample, allowing clear visualisation of microstructures and grain boundaries. Here, secondary austenite phases are indicated by black circles. However, analysis of the same region using EBSD phase mapping, as shown in Fig. 9(b), reveals that these phases were not effectively indexed despite the use of a fine step size. This suggests that the EBSD method may underestimate the austenite phase fraction. Consequently, the calculated volumetric fraction of austenite may not fully represent the accurate phase distribution, particularly in regions with a high prevalence of secondary austenite.

Fig. 10(a) illustrates the identification of CrN using EBSD analysis. Phase mapping with a fine step size of 0.1 μm revealed traces of CrN at ferrite-austenite interfaces and within the ferrite matrix. SEM images at different magnifications further highlight the coexistence of chromium nitrides and fine secondary austenitic structures within ferrite zones (Fig. 10(b)) and along the edges of austenite (Fig. 10(c)). Chromium nitrides, such as CrN and Cr_2N, play a crucial role in SDSS microstructural evolution. During cooling, these nitrides precipitate below 1000 °C due to nitrogen supersaturation in ferrite, serving as nucleation sites for IGA formation at temperatures below 650 °C. Upon reheating with the addition of new layers, nitrides partially dissolve at temperatures above 1000 °C, enriching the ferrite matrix with chromium and nitrogen, which facilitates the growth of GBA and WA in reheated regions [40]. The precipitation of chromium nitrides can significantly influence their mechanical properties and corrosion resistance. Chromium nitride precipitation enhances the hardness of the ferritic phase while negatively affecting fatigue resistance [41]. Furthermore, chromium nitride formation depletes the surrounding of chromium, creating localised areas with diminished corrosion resistance and making the material more susceptible to pitting and stress-corrosion cracking [42].

3.7. Microstructure evolution mechanism of SDSS during CW-GMA process

The microstructural evolution mechanism of SDSS during the CW-GMA deposition is illustrated in Fig. 11. Before adding the next layer, the wall predominantly displays a columnar ferrite structure, with equiaxed grains appearing at the transitions in the middle of the fusion line and along the wall edges. When adding a new layer, the melt pool forms from the fusion of the filler metal and the partial remelting of the previous layer [23]. The energy of the electric arc and the pressure of the plasma jet result in increased penetration in the central part of the melt pool, forming a penetration zone (PZ). The melt pool undergoes various cooling mechanisms, convection at the shielding gas and air interface, and conduction through the underlying layers. Conduction is particularly rapid and intense in the PZ, leading to faster initial solidification in this region. Additionally, Marangoni convection within the melt pool promotes heat accumulation along the lateral edges of the wall [43], making cooling at the PZ faster than the sides of the wall. As columnar ferrite grains nucleate along the liquidus transition and grow towards the centre, equiaxed ferrite grains will form at the centre due to higher cooling, resulting in smaller ferrite grains in the PZ [44]. At the same time, in the PZ, where rapid cooling and solidification occur, nitrogen tends to migrate out of the solidifying ferrite into the adjacent liquid metal, as ferrite can only dissolve about one-quarter of the nitrogen compared to the liquid phase. This process results in a depletion of nitrogen in the penetration zone and an enrichment in regions that cool more slowly [45]. Consequently, nitrogen accumulation in slower-cooling areas can facilitate the precipitation of secondary phases, such as Cr_2N and CrN, which support the nucleation of IGA at later cooling stages. Once stabilised, the solidification front becomes homogenised through diffusion and advances uniformly along BD, parallel to the thermal gradient. This promotes the growth of coarse columnar ferrite grains aligned along the <001> direction, following the thermal gradient. These columnar grains extend to meet the solidification front near the wall edges, shaped by convection within the melt pool, forming a layer of fine ferrite grains on the surface.

The evolution of microstructure during the CW-GMA process for SDSS is illustrated in Fig. 11(b). At the liquidus temperature (1460 °C), the rapid solidification of the melt pool results in the formation of δ-ferrite, characterised by large columnar grains formed through epitaxial growth. As the temperature decreases between 1350 °C and 800 °C, GBA nucleates along δ/δ grain boundaries. In colder AM processes such as laser or plasma deposition, the rapid cooling following reheating leads to nitrogen supersaturation in ferrite. Under these conditions, nitrogen cannot diffuse into austenite due to the limited diffusion time, which promotes the formation of chromium nitrides within the δ-ferrite grains [46–48]. However, in hotter processes such as WDED, the nitrogen precipitation is often delayed by several passes due to the loss of nitrogen in the air [49]. Indeed, studies have shown that the microstructure is strongly affected by successive reheating cycles, primarily due to a decrease in nitrogen content. Nitrogen is the only element whose concentration is significantly influenced by the deposition, and its concentration can greatly decrease depending on the number of successive passes and the energy input employed during the process [50]. CrN forms as an initial metastable phase in the precipitation process of chromium nitrides, providing nucleation sites for the

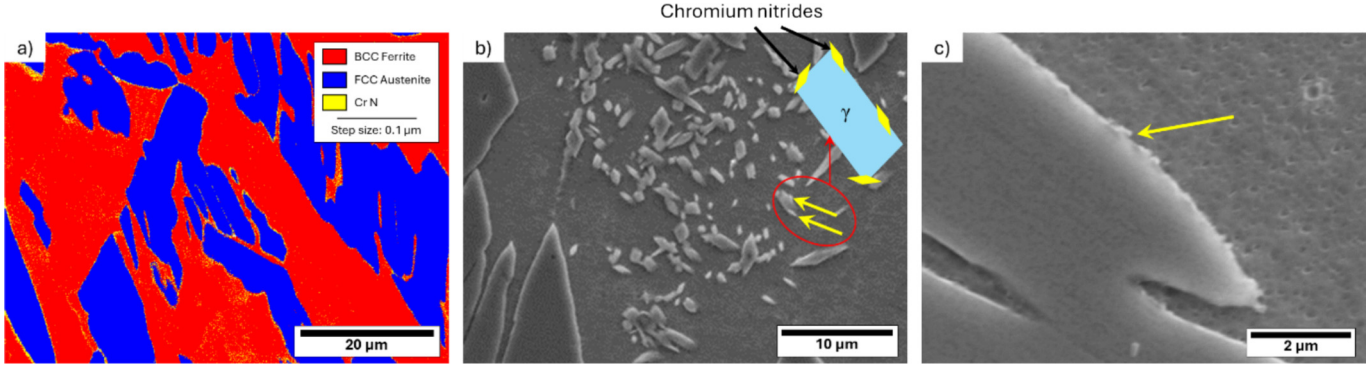


Fig. 10. Identification of CrN using EBSD analysis a), SEM image of fine secondary austenite region b) and high magnification austenite grain boundary c). Chromium nitrides indicated by yellow arrows. (For interpretation of the references to colour in this figure legend, the reader is referred to the web version of this article.)

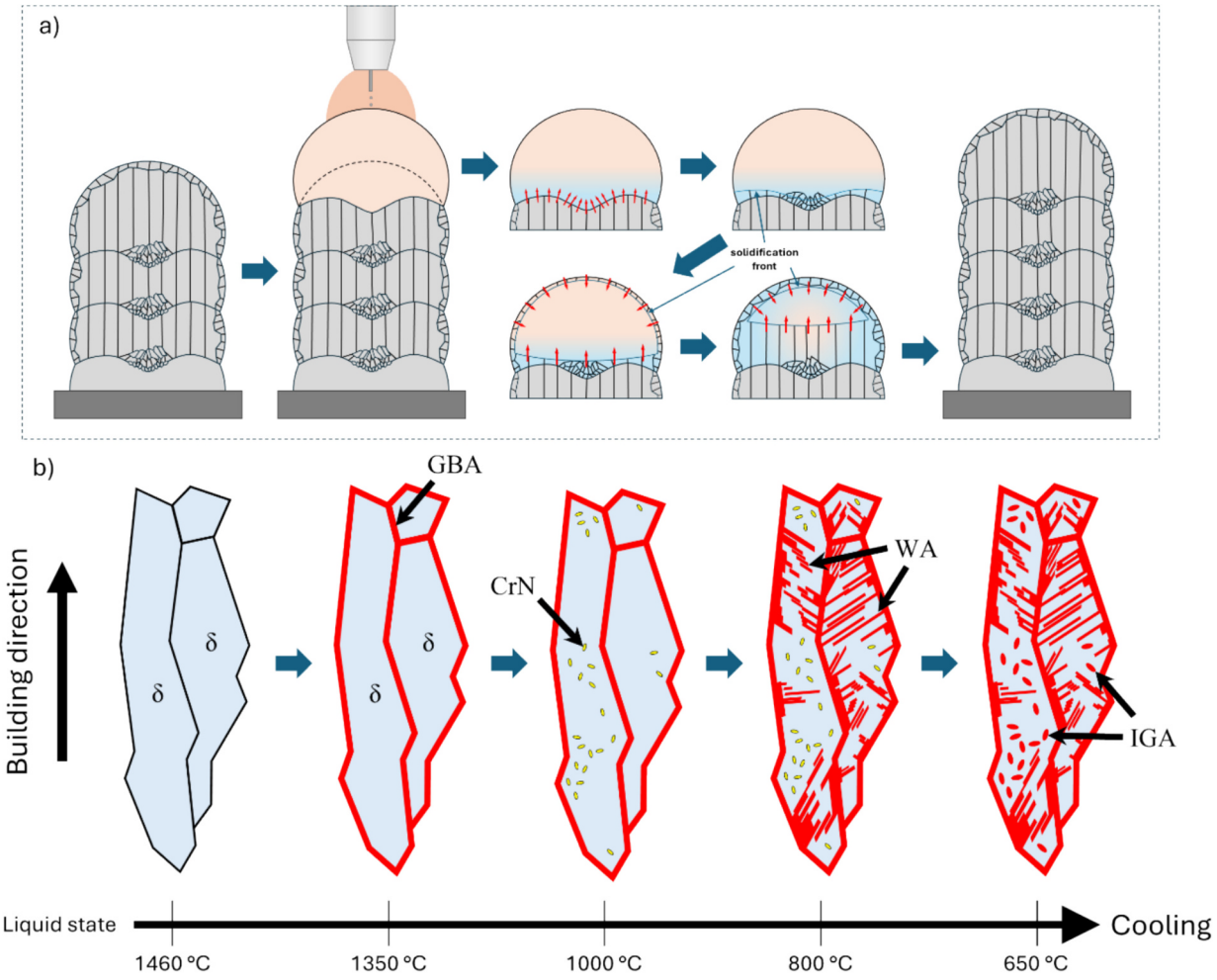


Fig. 11. a) Schematic representation of ferrite grain growth during the CW-GMA process for SDSS, b) Schematic representation of microstructure evolution during cooling in the CW-GMA process for SDSS.

thermodynamically more stable Cr_2N [51]. This is why, in hot AM processes, only few stable nitrides precipitation can be observed. At 800 °C, WA nucleates epitaxially from GBA and grows into ferrite grains in a lath-like structure. This epitaxial growth is driven by the alignment of grains within the δ-ferrite phase, which provides favourable conditions for the transformation. When the temperature falls below 650 °C, IGA nucleates on inclusion, such as oxides and chromium nitrides. These precipitates create localised compositional and strain fields that facilitate the initiation of IGA. Furthermore, chromium depletion in the surrounding matrix stabilises secondary austenite in these regions.

3.8. Mechanical properties

Fig. 12(a) presents the microhardness profiles for SDSS walls

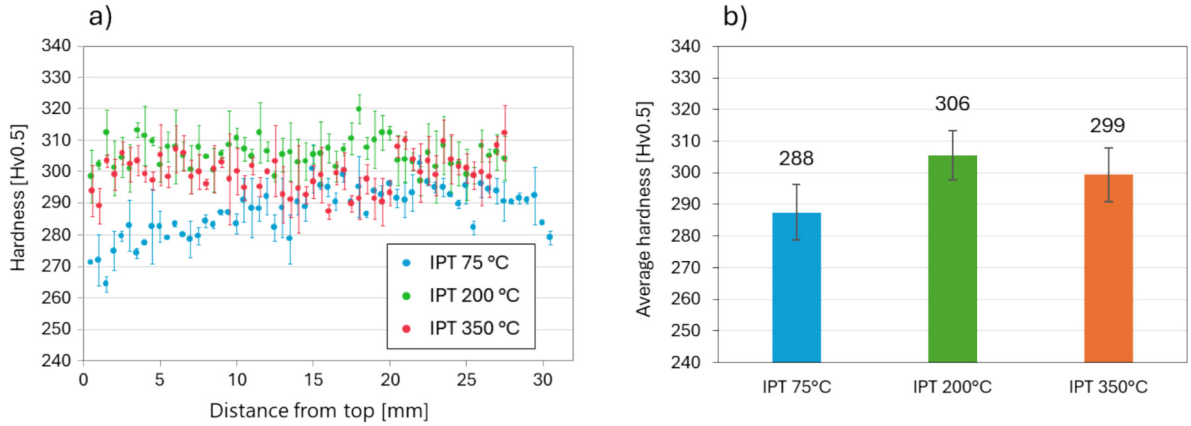


Fig. 12. a) Micro-hardness profile of SDSS CW-GMA process walls.
b) average hardness with different interpass temperatures.

deposited using the CW-GMA process. Each curve represents the average hardness measured along three central lines of the cross-section for each wall. Fig. 12(b) shows the average microhardness values for each IPT condition. The recorded values were 287 Hv for the IPT 75 °C wall, 305 Hv for the IPT 200 °C wall, and 299 Hv for the IPT 350 °C wall, which are close to the typical hardness of UNS S32906 SDSS at 312 Hv [52]. The hardness profile for the 75 °C IPT wall starts at 270 Hv near the surface and gradually increases to around 295 Hv towards the mid-section, aligning with the hardness range of the other conditions. This gradient suggests a surface-softening effect in the lower IPT condition, potentially caused by thermal gradients or limited austenite precipitation near the surface. In contrast, the hardness profiles for the 200 °C and 350 °C IPT walls remain uniform throughout their cross-sections, fluctuating slightly around 300 Hv and 305 Hv, respectively. This uniformity reflects a stable microstructure across the wall height in these samples. Although the differences between the average hardness values at each IPT are modest, the data suggests a trend towards slightly increased hardness with higher IPTs. This could indicate enhanced precipitation of austenitic phases or a more refined ferritic matrix at elevated IPTs, improving hardness uniformity.

Fig. 13(a, b) present the stress-strain curves and average from tensile tests conducted on nine specimens extracted from each wall. For each IPT, the stress-strain curve is displayed with solid, dashed, and dotted lines grouped by colour. The average yield strength (YS) and ultimate tensile strength (UTS) across the three groups are similar, measuring 629.4 ± 11.9 MPa and 810.6 ± 2.9 MPa, respectively. These results exceed the typical mechanical properties reported of UNS S32906, which are 550 MPa and 750 MPa [53]. This enhancement is likely due to the as-deposited microstructure produced by the CW-GMA process, which can lead to grain refinement with high dislocation density. The repeatability of these results indicates that the effect of IPT on mechanical properties is minimal. Furthermore, the relatively low standard deviation observed for YS and UTS highlights the high consistency of the mechanical performance of the samples. This suggests that the CW-GMA process produces SDSS walls with reliable strength characteristics. The dotted lines correspond to samples exhibiting the lowest elongation, with a minimum elongation of 16 % observed at an IPT of 350 °C. This reduced elongation can be attributed to porosities in tensile specimens, which will be further examined in the fracture surface analysis. Tensile properties reported in the literature for SDSS produced by various manufacturing methods are summarised in Table 2. The properties obtained in this study fall within the upper range of values reported in the literature, with UTS values exceeding 800 MPa and elongation reaching over 25 %.

The fracture surfaces of tensile-tested SDSS samples, produced with the CW-GMA process at varying IPT, are presented in Fig. 14 and Fig. 15. Fig. 14 shows fracture areas for each IPT condition, with images captured at low (a–c) and high magnifications (d–j). At lower magnifications, the fracture surfaces exhibit the same characteristic, entirely composed of dimples, suggesting a ductile fracture behaviour regardless of the IPT. Closer examination of the surface revealed the occasional presence of secondary cracks. Compared with colder processes characterised by higher cooling rates, such as laser powder bed fusion (LPBF), the fracture surfaces from CW-GMA samples display a much lower density of secondary cracks. In LPBF-processed samples, secondary cracks are often associated with pre-existing porosity [59]. An EDS analysis was conducted on one inclusion to further investigate the inclusions observed on the fracture surfaces (Fig. 14(g)). The chemical composition of this inclusion was found to be Cr 43.6 %, Ni 3.4 %, and Mn 3.3 %. The high chromium content, combined with minor amounts of nickel and manganese, suggests that this inclusion could correspond to impurities or chromium carbides formed during solidification or thermal cycling. Such inclusions are known to concentrate stress, which could contribute to the initiation of secondary cracks under tensile loading.

Porosity and lack of fusion are frequent defects in the additive manufacturing of DSS and must be reduced due to their detrimental impact on material properties. In Fig. 15, fracture surfaces from samples exhibiting significant porosity and lack of fusion, correlating with lower elongation values (16 % and 22 %), are displayed to highlight the effects of process-induced defects on mechanical response. For samples with lack of fusion voids, these regions are accompanied by extensive cleavage plains indicative of brittle fracture, with sharp and planar break surfaces. According to [55], the growth and coalescence of porosities, alongside the initiation and propagation of secondary cracks, substantially affect the total elongation of SDSS samples.

Despite differences in pore size, ranging from 250 μm for samples at 350 °C to up to 1 mm in the 75 °C samples, the 350 °C IPT sample exhibited lower elongation. This suggests that, beyond pore size, other factors, such as cleavage, also influence mechanical properties. Upon closer examination, the cleavage surfaces of samples at 75 °C and 200 °C reveal ribbed fracture surfaces interspersed with small ductile zones. By contrast, the cleavage region in the 350 °C sample is more uniform and exhibits a cleaner, continuous fracture surface, indicative of a more brittle behaviour under tensile loading. Although these voids act as crack initiation sites, especially under tensile stress, the UTS and YS values remain consistent with those observed in samples without visible defects. Additional cold deformation processes such as peening or rolling may be employed to densify the material and reduce internal voids during the build to mitigate porosity formation.

4. Conclusion

This study examined the impact of IPT on the microstructure, mechanical properties, and phase transformations of SDSS fabricated using the CW-GMA additive manufacturing method. The main findings are

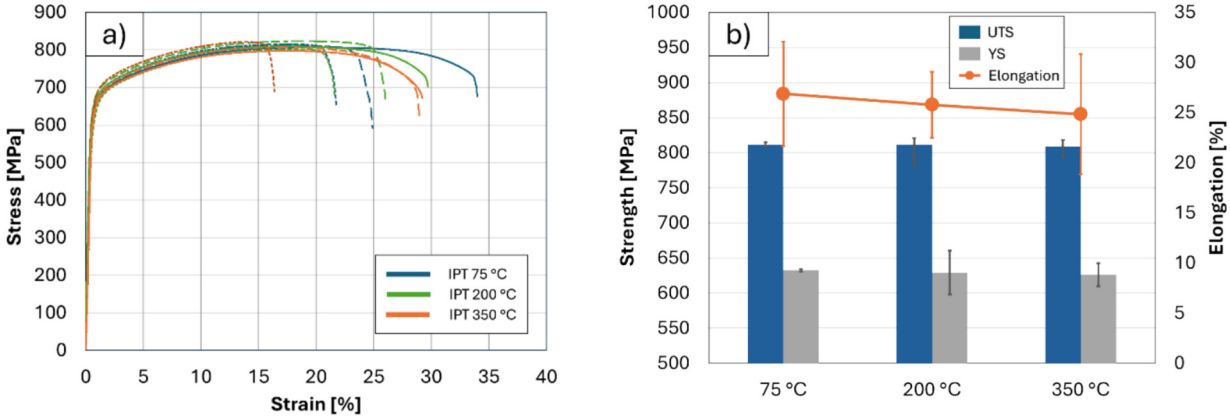


Fig. 13. a) Room temperature tensile results of SDSS CW-GMA a) Stress-strain curve, b) Average UTS, YS, and elongation results at different interpass temperatures.

Table 2
Summary of tensile test properties of SDSS produced by different deposition and forming methods.

Material	PREN	Process	Condition	UTS [MPa]	YS [MPa]	EL [%]	Ref
UNS S32906	42	WDED: CW-GMA	As-deposited	812 ± 8.9	634 ± 25.7	26 ± 5.1	This study
	42	Hot rolled	As-rolled	931	708	39.7	[54]
SAF 2209	36	WDED: GMA	As-deposited	770.1 ± 32.7	507.5 ± 2.9	35 ± 3.8	[55]
	36	WDED:					[56]
		GMA	As-deposited	770 ± 28.3	580 ± 19.8	57 ± 2.5	
		CMT	As-deposited	832 ± 8.5	610 ± 2.8	63 ± 0.4	
UNS S32750	36	WDED: CMT	As-deposited	796	680	25.2	[14]
	40	WDED: GTA	As-deposited	~550	~900	~34	[57]
	43	LDED	As-deposited	950 ± 21	820 ± 35	15 ± 3	[58]
	41	LPBF	As-deposited	1485 ± 6	1265 ± 22	7 ± 0	[59]
			Annealed	925 ± 3	615 ± 5	34 ± 0	
	42	LPBF	As-deposited	801.5 ± 12.5	691.7 ± 27.4	18 ± 2.6	[60]
			Annealed	789.4 ± 15.2	545.0 ± 22.1	45 ± 2.4	
	41	Hot rolled	As-rolled	935 ± 2	772 ± 1	44 ± 0.6	[61]
FCWA-AM	46	WDED: GMA	As-deposited	809 ± 12	961 ± 5	N/A	[23]

PREN: Pitting resistance equivalent number.
WDED: Wire-arc direct energy deposition.
CMT: Cold metal transfer.
GTA: Gas tungsten arc.
LDED: Laser-direct energy deposition.
L-PBF: Laser powder bed fusion.
FCWA-AM: flux-cored wire arc additive manufacturing.

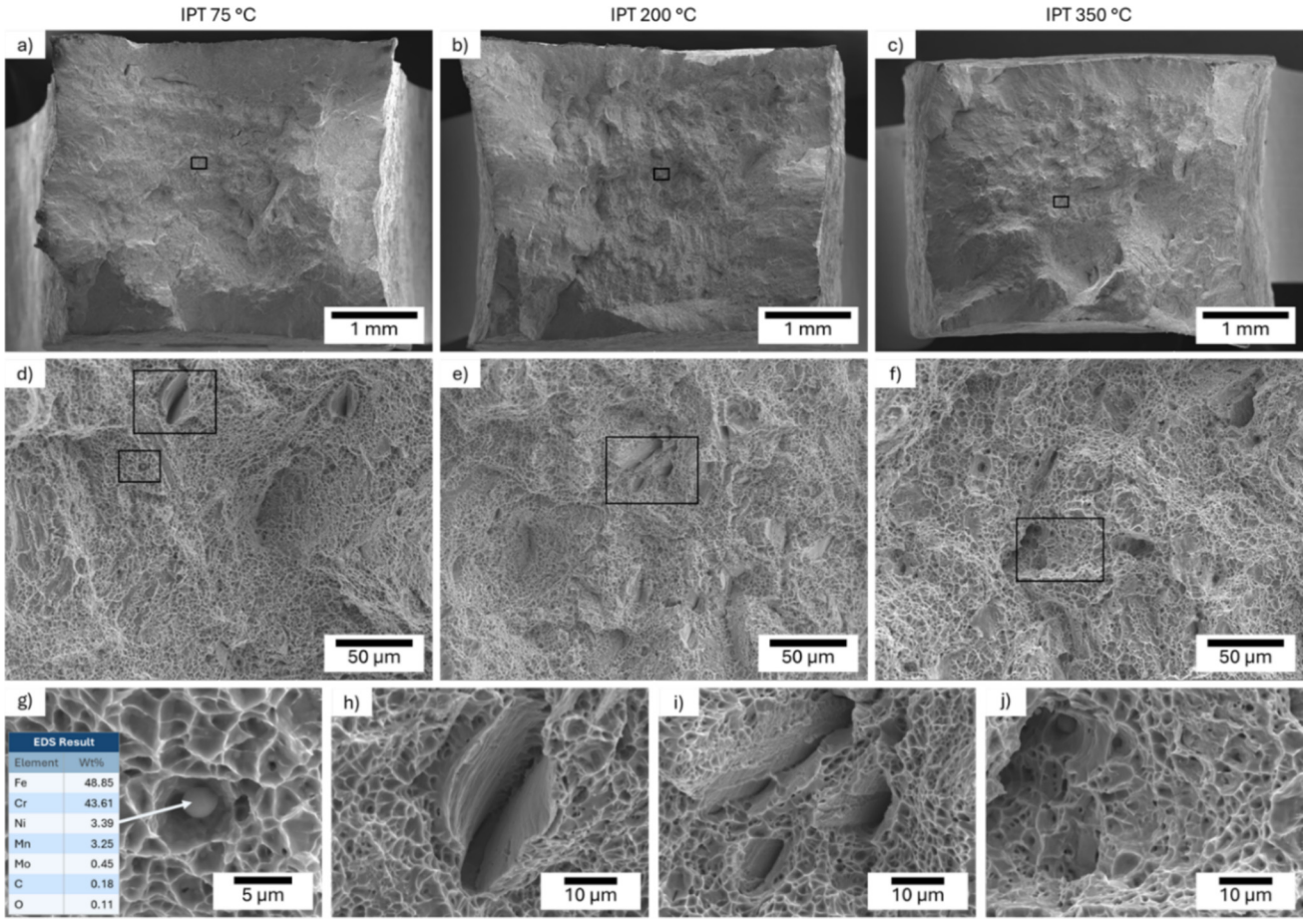


Fig. 14. Fracture morphology of tensile specimens at difference magnifications (a, d, g, h) IPT of 75 °C (b, e, i) IPT of 200 °C (c, f, j) IPT of 350 °C.

summarised as follows:

- Higher IPTs, such as 350 °C, led to shorter interpass dwell times and greater thermal accumulation, increasing exposure to high temperatures.
- The microstructure transitioned from coarse δ-ferrite grains at high temperatures to a mix of austenitic phases (GBA, WA, and IGA) and secondary nitrides (CrN and Cr_2N) at lower temperatures. Higher IPTs promoted secondary austenite formation and nitride precipitation, particularly in the penetration zone. Despite these local

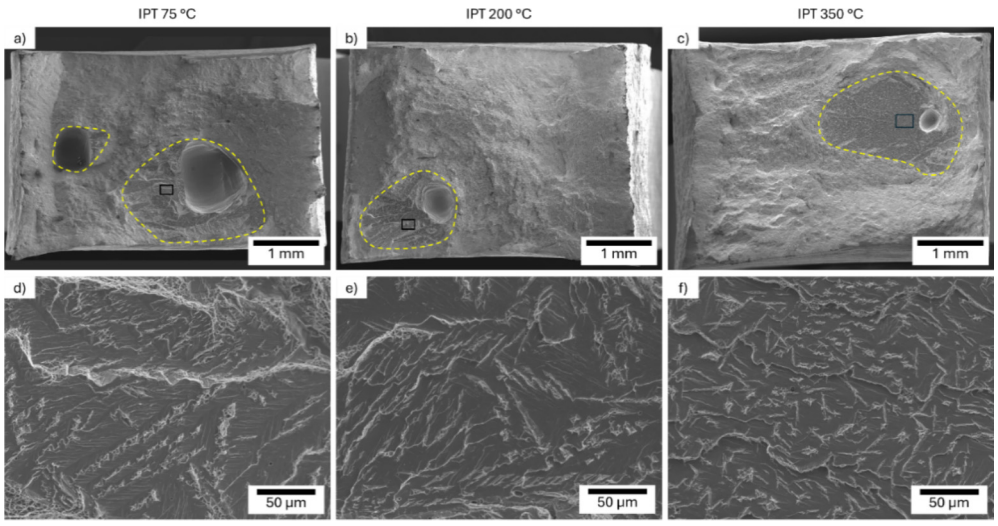


Fig. 15. Fracture morphology of tensile specimens with low elongation at difference magnifications (a, d) IPT of 75 °C (b, e) IPT of 200 °C (c, f) IPT of 350 °C.

changes, the overall ferrite-austenite phase ratio remained stable, with no significant variation in the volumetric austenite fraction.
- EBSD analysis indicated strong ferritic grain alignment along <001>, parallel to the thermal gradient, across all IPT conditions.
- Hardness values of 300 Hv and UTS of 810 MPa remained consistent across all IPTs, with slightly improved hardness uniformity observed at higher IPTs.

These findings show that while IPT influences thermal accumulation and local microstructural features close to reheated region, it has minimal impact on the overall phase ratio and mechanical properties, demonstrating the robustness of the CW-GMA process for producing SDSS components with reliable and consistent performance. Further studies will be conducted to minimise process-induced porosity through gas shielding and in-process deformation strategies.

CRediT authorship contribution statement

P. Poulain: Writing – original draft, Investigation. **J. Wang:** Writing – review & editing, Supervision, Project administration, Methodology, Investigation. **S. Bouvier:** Writing – review & editing, Supervision, Methodology, Formal analysis. **S. Williams:** Writing – review & editing, Supervision, Resources, Project administration, Funding acquisition. **S. Budnyk:** Writing – review & editing, Resources, Project administration, Funding acquisition. **A. Gavrilovic-Wohlmuther:** Writing – review & editing, Resources, Project administration, Funding acquisition.

Declaration of competing interest

The authors declared that they have no conflicts of interest and have no commercial or associative interest that represents a conflict of interest in connection with the work submitted.

Acknowledgements

The author expresses gratitude to Christof Group SBN for initiating the project and providing financial support. Special thanks to Cranfield University technical team, especially Nisar Shah, Steve Pope, Tracey Roberts, and Kris Bramley, for their invaluable assistance with the deposition process, as well as the metallographic and EBSD experiments.

References

[1] Harris Ian D. Development and implementation of metals additive manufacturing. 2017.
[2] Laureijs RE, Roca JB, Narra SP, Montgomery C, Beuth JL, Fuchs ERH. Metal additive manufacturing: cost competitive beyond low volumes. J Manuf Sci E T ASME Aug. 2017;139(8). https://doi.org/10.1115/1.4035420.
[3] Herzog D, Seyda V, Wycisk E, Emmelmann C. Additive manufacturing of metals. Acta Mater Sep. 2016;117:371–92. https://doi.org/10.1016/j.actamat.2016.07.019.
[4] Srivastava M, Rathee S, Tiwari A, Dongre M. Wire arc additive manufacturing of metals: a review on processes, materials and their behaviour. Mater Chem Phys Jan. 2022:126988. https://doi.org/10.1016/j.matchemphys.2022.126988.
[5] Costello SCA, Cunningham CR, Xu F, Shokrani A, Dhokia V, Newman ST. The state-of-the-art of wire arc directed energy deposition (WA-DED) as an additive manufacturing process for large metallic component manufacture. Int J Comput Integr Manuf 2023;36(3):469–510. https://doi.org/10.1080/0951192X.2022.2162597.
[6] Wang C, et al. A novel cold wire gas metal arc (CW-GMA) process for high productivity additive manufacturing. Addit Manuf Jul. 2023;73. https://doi.org/10.1016/j.addma.2023.103681.
[7] Stützer J, Totzauer T, Wittig B, Zinke M, Jüttner S. GMAW cold wire technology for adjusting the ferrite–austenite ratio of wire and arc additive manufactured duplex stainless steel components. Metals (Basel) May 2019;9(5). https://doi.org/10.3390/met9050564.
[8] Boillot P, Peultier J. Use of stainless steels in the industry: recent and future developments. Procedia Engineering 2014:309–21. https://doi.org/10.1016/j.proeng.2014.09.015. Elsevier Ltd.
[9] L. Karlsson and H. Arcini, "Low energy input welding of duplex stainless steels.".
[10] Haldorsen LM, et al. Recent experiences with cracking of load bearing dissimilar metal welds on subsea production systems [Online]. Available: http://asmedigitalcollection.asme.org/OMAE/proceedings-pdf/OMAE2017/57687/V004T03A029/2571420/v004t03a029-omae2017-61176.pdf.
[11] Bachiri A, Badji R, Touhami M Zine, Gharbi A, Ghelloudj O, Remili S. Influence of thermomechanical treatment on the structure, hardness and corrosion behavior of super duplex stainless steel. Mater Today Proc 2023. https://doi.org/10.1016/j.matpr.2023.03.418.
[12] Zhang D, Liu A, Yin B, Wen P. Additive manufacturing of duplex stainless steels – a critical review. Jan. 01. Elsevier Ltd.; 2022. https://doi.org/10.1016/j.jmapro.2021.11.036.
[13] Sales A, Kotousov A, Yin L. Design against fatigue of super duplex stainless steel structures fabricated by wire arc additive manufacturing process. Metals (Basel) Dec. 2021;11(12). https://doi.org/10.3390/met11121965.
[14] Huang X, et al. Anisotropic behavior of super duplex stainless steel fabricated by wire arc additive manufacturing. J Mater Res Technol Nov. 2023;27:1651–64. https://doi.org/10.1016/j.jmrt.2023.10.005.
[15] Knezović N, Garašić I, Jurić I. Influence of the interlayer temperature on structure and properties of wire and arc additive manufactured duplex stainless steel product. Materials Dec. 2020;13(24):1–16. https://doi.org/10.3390/ma13245795.
[16] Stützer J, Zinke M, Jüttner S. Studies on the pore formation in super duplex stainless steel welds. Welding in the World Mar. 2017;61(2):351–9. https://doi.org/10.1007/s40194-016-0409-6.
[17] Mohammed GR, Ishak M, Aqida SN, Abdulhadi HA. Effects of heat input on microstructure, corrosion and mechanical characteristics of welded austenitic and duplex stainless steels: a review. Feb. 01. MDPI AG; 2017. https://doi.org/10.3390/met7020039.
[18] Higelin A, Le Manchet S, Passot G, Cissé S, Grocki J. Heat-affected zone ferrite content control of a duplex stainless steel grade to enhance weldability. Welding in the World Aug. 2022;66(8):1503–19. https://doi.org/10.1007/s40194-022-01326-0.

[19] Hosseini VA, Karlsson L, Wessman S, Fuertes N. Effect of sigma phase morphology on the degradation of properties in a super duplex stainless steel. Materials Jun. 2018;11(6). https://doi.org/10.3390/ma11060933.
[20] Rodriguez-Vargas BR, Stornelli G, Di Schino A, Pérez AFM. Influence of GTAW shielding gas on the microstructure of duplex stainless steel-welded joints. MRS Adv Dec. 2024. https://doi.org/10.1557/s43580-024-00980-4.
[21] Lervåg M, et al. Additive manufacturing with superduplex stainless steel wire by cmt process. Metals (Basel) Feb. 2020;10(2). https://doi.org/10.3390/met10020272.
[22] Yang Y, et al. Effect of a brief post-weld heat treatment on the microstructure evolution and pitting corrosion of laser beam welded UNS S31803 duplex stainless steel. Corros Sci Dec. 2012;65:472–80. https://doi.org/10.1016/j.corsci.2012.08.054.
[23] Zhang Y, Wu S, Cheng F. A specially-designed super duplex stainless steel with balanced ferrite:austenite ratio fabricated via flux-cored wire arc additive manufacturing: microstructure evolution, mechanical properties and corrosion resistance. Mater Sci Eng A Sep. 2022;854. https://doi.org/10.1016/j.msea.2022.143809.
[24] Xavier CR, Delgado HG, Rebello MG, Lisbôa RR, Silva ACM, de Castro JA. Numerical prediction for the effects of welding Interpass temperature on the thermal history and microstructure of duplex stainless steels. Materials Research 2023;26. https://doi.org/10.1590/1980-5373-MR-2022-0529.
[25] "Designation: E8/E8M − 13a standard test methods for tension testing of metallic materials 1", doi: https://doi.org/10.1520/E0008_E0008M-13A.
[26] Xu M, Chen S, Yuan T, Jiang X, Zhang H. Effect of thermal cycles on the microstructure and properties of the Al–Zn–Mg–Cu alloy during wire-arc additive manufacturing. J Alloys Compd Dec. 2022;928. https://doi.org/10.1016/j.jallcom.2022.167172.
[27] Pixner F, et al. Thermal cycling effects on the local microstructure and mechanical properties in wire-based directed energy deposition of nickel-based superalloy. Addit Manuf Mar. 2024;83. https://doi.org/10.1016/j.addma.2024.104066.
[28] Pixner F, et al. Influence of process and heat input on the microstructure and mechanical properties in wire arc additive manufacturing of hot work tool steels. Mater Sci Eng A Nov. 2023;888. https://doi.org/10.1016/j.msea.2023.145799.
[29] Rodrigues TA, Duarte V, Avila JA, Santos TG, Miranda RM, Oliveira JP. Wire and arc additive manufacturing of HSLA steel: effect of thermal cycles on microstructure and mechanical properties. Addit Manuf May 2019;27:440–50. https://doi.org/10.1016/j.addma.2019.03.029.
[30] Zhai W, Wu N, Zhou W. Effect of interpass temperature on wire arc additive manufacturing using high-strength metal-cored wire. Metals (Basel) Feb. 2022;12(2). https://doi.org/10.3390/met12020212.
[31] Wang J, et al. Evolution of crystallographic orientation, precipitation, phase transformation and mechanical properties realized by enhancing deposition current for dual-wire arc additive manufactured Ni-rich NiTi alloy. Addit Manuf Aug. 2020;34. https://doi.org/10.1016/j.addma.2020.101240.
[32] Hosseini V. Super duplex stainless steels-microstructure and properties of physically simulated base and weld metal. 2018.
[33] Ramirez AJ, Brandi SD, Lippold JC. Secondary austenite and chromium nitride precipitation in simulated heat affected zones of duplex stainless steels. Science and Technology of Welding and Joining Aug. 2004;9(4):301–13. https://doi.org/10.1179/136217104225021715.
[34] Zhang Y, Cheng F, Wu S. Improvement of pitting corrosion resistance of wire arc additive manufactured duplex stainless steel through post-manufacturing heat-treatment. Mater Charact Jan. 2021;171. https://doi.org/10.1016/j.matchar.2020.110743.
[35] Salahi S, Nemani AV, Ghaffari M, Lunde J, Nasiri A. On microstructure, crystallographic orientation, and corrosion properties of wire arc additive manufactured 420 martensitic stainless steel: effect of the inter-layer temperature. Addit Manuf Oct. 2021;46. https://doi.org/10.1016/j.addma.2021.102157.
[36] Karlsson L, Börjesson J. Orientation relationships of intragranular austenite in duplex stainless steel weld metals. Science and Technology of Welding and Joining 2014;19(4):318–23. https://doi.org/10.1179/1362171813Y.0000000192.
[37] Menezes JWA, Abreu H, Kundu S, Bhadeshia HKDH, Kelly PM. Crystallography of Widmanstätten austenite in duplex stainless steel weld metal. Science and Technology of Welding and Joining Jan. 2009;14(1):4–10. https://doi.org/10.1179/136217108X341166.
[38] Attar HZ, Fellowes JW, Roy MJ, Hosseini VA, Engelberg DL. Optimizing the phase distribution in arc-based direct energy deposition of duplex stainless steel. Metall Mater Trans A Phys Metall Mater Sci May 2024;55(5):1600–25. https://doi.org/10.1007/s11661-024-07355-2.
[39] Prathivraj S, Oyyaravelu R. Effect of interpass temperature on austenite ferrite ratio of wire arc additive manufactured 2507 super duplex stainless steel. Mater Lett Apr. 2024;361. https://doi.org/10.1016/j.matlet.2024.136125.
[40] A. J. Ramirez, J. C. Lippold, and S. D. Brandi, "The relationship between chromium nitride and secondary austenite precipitation in duplex stainless steels.".
[41] Hereñú S, Moscato MG, Alvarez I, Armas AF. The influence of chromium nitrides precipitation on the fatigue behavior of duplex stainless steels. Procedia Engineering 2014:179–82. https://doi.org/10.1016/j.proeng.2014.06.246. Elsevier Ltd.
[42] Ito M, et al. Identification of chromium-depleted area around chromium nitride precipitates in heat-affected zone of lean-duplex stainless steel and in-situ observation of preferential dissolution by EC-AFM. ISIJ International 2022;62(3):568–76. https://doi.org/10.2355/isijinternational.ISIJINT-2021-462.
[43] Liu D, Wu D, Wang R, Shi J, Niu F, Ma G. Formation mechanism of Al-Zn-Mg-Cu alloy fabricated by laser-arc hybrid additive manufacturing: microstructure evaluation and mechanical properties. Addit Manuf Feb. 2022;50. https://doi.org/10.1016/j.addma.2021.102554.
[44] Gao M, Zeng X, Yan J, Hu Q. Microstructure characteristics of laser-MIG hybrid welded mild steel. Appl Surf Sci Jul. 2008;254(18):5715–21. https://doi.org/10.1016/j.apsusc.2008.03.070.
[45] "Weldability of high nitrogen stainless steel".
[46] Taban E. Toughness and microstructural analysis of superduplex stainless steel joined by plasma arc welding. J Mater Sci Jun. 2008;43(12):4309–15. https://doi.org/10.1007/s10853-008-2632-z.
[47] Taban E, Kaluc E. Welding behaviour of duplex and superduplex stainless steels using laser and plasma arc welding processes. 2011.
[48] Chen TH, Yang JR. Microstructural characterization of simulated heat affected zone in a nitrogen-containing 2205 duplex stainless steel [Online]. Available: www.elsevier.com/locate/msea.
[49] Hosseini VA, Valiente Bermejo MA, Gårdstam J, Hurtig K, Karlsson L. Influence of multiple thermal cycles on microstructure of heat-affected zone in TIG-welded super duplex stainless steel. Welding in the World Feb. 2016;60(2):233–45. https://doi.org/10.1007/s40194-016-0300-5.
[50] Hosseini Vahid A. Influence of multiple welding cycles on microstructure and corrosion resistance of a super duplex stainless steel [Online]. Available: https://www.researchgate.net/publication/311079859; 2016.
[51] Holländer Pettersson N, Lindell D, Lindberg F, Borgenstam A. Formation of chromium nitride and intragranular austenite in a super duplex stainless steel. Metall Mater Trans A Phys Metall Mater Sci 2019;50(12):5594–601. https://doi.org/10.1007/s11661-019-05489-2.
[52] "Practical guide to using duplex stainless steels.".
[53] "Standard Specification for Stainless Steel Bars and Shapes for Use in Boilers and Other Pressure Vessels".
[54] Lillbacka R, Chai G, Ekh M, Liu P, Johnson E, Runesson K. Cyclic stress-strain behavior and load sharing in duplex stainless steels: aspects of modeling and experiments. Acta Mater Sep. 2007;55(16):5359–68. https://doi.org/10.1016/j.actamat.2007.05.056.
[55] Hejripour F, Binesh F, Hebel M, Aidun DK. Thermal modeling and characterization of wire arc additive manufactured duplex stainless steel. J Mater Process Technol Oct. 2019;272:58–71. https://doi.org/10.1016/j.jmatprotec.2019.05.003.
[56] Bellamkonda PN, Dwivedy M, Sudersanan M, Visvalingam B. Influence of welding processes on the microstructure and mechanical properties of duplex stainless steel parts fabricated by wire arc additive manufacturing. Metals and Materials International Feb. 2024. https://doi.org/10.1007/s12540-024-01753-2.
[57] Zhang X, et al. Microstructure and mechanical properties of TOP-TIG-wire and arc additive manufactured super duplex stainless steel (ER2594). Mater Sci Eng A Aug. 2019;762. https://doi.org/10.1016/j.msea.2019.138097.
[58] Jiang D, Gao X, Zhu Y, Hutchinson C, Huang A. In-situ duplex structure formation and high tensile strength of super duplex stainless steel produced by directed laser deposition. Mater Sci Eng A Jan. 2022;833. https://doi.org/10.1016/j.msea.2021.142557.
[59] Karavias L, Gargalis L, Graff JS, Johansen M, Diplas S, Karaxi EK. Tensile properties and fracture analysis of duplex (2205) and super duplex (2507) stainless steels, produced via laser powder bed fusion additive manufacturing. Metals (Basel) Jul. 2024;14(7). https://doi.org/10.3390/met14070838.
[60] Cao F, et al. Effect of inhomogeneous fiber structure on the mechanical properties of friction stir welded SAF 2507 super duplex stainless steel. Mater Chem Phys May 2022;283. https://doi.org/10.1016/j.matchemphys.2022.126026.
[61] Gupta MK, Singh NK, Gupta NK. Deformation behaviour and notch sensitivity of a super duplex stainless steel at different strain rates and temperatures. Int J Impact Eng Apr. 2023;174. https://doi.org/10.1016/j.ijimpeng.2023.104494.

DSPACE

https://dspace.org/

Impact of interpass temperature on the microstructure and mechanical properties of super duplex stainless steel in CW-GMA additive manufacturing

Poulain, Paul; Wang, Jun; Bouvier, Salima; Williams, Stewart W.; Budnyk, Sergij L. ...

2025-07-30
Elsevier
https://doi.org/10.1016/j.jmapro.2025.04.091
Poulain P, Wang J, Bouvier S, et al., (2025) Impact of interpass temperature on the microstructure and mechanical properties of super duplex stainless steel in CW-GMA additive manufacturing. Journal of Manufacturing Processes, Volume 146, July 2025, pp. 30-43

Downloaded from a DSpace repository. https://dspace.org/